Journal of the Electrochemical Society

Effective Upcycling of Graphite Anode: Healing and Doping Enabled Direct Regeneration

Journal of The Electrochemical Society, 2020 **167** 160511

Effective Upcycling of Graphite Anode: Healing and Doping Enabled Direct Regeneration

Brandon Markey,[1] Minghao Zhang,[1,*] Iva Robb,[1] Panpan Xu,[1,z] Hongpeng Gao,[2] Dawei Zhang,[2] John Holoubek,[1] David Xia,[1] Yifan Zhao,[3] Juchen Guo,[3,4,] Mei Cai,[5] Ying Shirley Meng,[1,2,6,***] and Zheng Chen[1,2,6,7,**,z]**

[1]*Department of NanoEngineering, University of California, San Diego, La Jolla, CA 92093, United States of America*
[2]*Program of Materials Science and Engineering, University of California, Riverside, Riverside, CA 92521, United States of America*
[3]*Program of Materials Science and Engineering, University of California, Riverside, Riverside, CA 92521, United States of America*
[4]*Department of Chemical and Environmental Engineering, University of California, Riverside, Riverside, CA 92521, United States of America*
[5]*General Motors Research and Development Center, Warren, MI 48092, United States of America*
[6]*Sustainable Power and Energy Center, University of California, San Diego, La Jolla, CA 92093, United States of America*
[7]*Program of Chemical Engineering, University of California, San Diego, La Jolla, CA 92093, United States of America*

As lithium-ion batteries (LIBs) become vital energy source for daily life and industry applications, a large volume of spent LIBs will be produced after their lifespan. Recycling of LIBs has been considered as an effective closed-loop solution to mitigate both environmental and economic issues associated with spent LIBs. While reclaiming of transition metal elements from LIB cathodes has been well established, recycling of graphite anodes has been overlooked. Here, we show an effect upcycling method involving both healing and doping to directly regenerate spent graphite anodes. Specifically, using boric acid pretreatment and short annealing, our regeneration process not only heals the composition/structure defects of degraded graphite but also creates functional boron-doping on the surface of graphite particles, providing high electrochemical activity and excellent cycling stability. The efficient direct regeneration of spent graphite by using low cost, non-volatile and non-caustic boric acid with low annealing temperature provides a more promising direction for green and sustainable recycling of spent LIB anodes.
 [DOI: 10.1149/1945-7111/abcc2f]

Manuscript submitted September 26, 2020; revised manuscript received October 28, 2020. Published November 30, 2020.

Supplementary material for this article is available online

Lithium-ion batteries (LIBs) have been extensively used as the power source for portable electronics and electric vehicles (EVs) because of their high energy density and long cycle life.[1] It is projected that the global LIBs production will reach ~440 GWh by 2025, corresponding to a market value of ~$100 billion USD.[2] Since the typical life-span of LIBs is 3–10 years, a large amounts of LIBs will be retried in the near future.[3] Like the global plastic waste issues we are facing today, if immediate actions were not taken, such battery wastes will pose grand challenge to our society. In this context, recycling is regarded as an effective closed-loop solution to mitigate environmental issues associated with inappropriate disposal of spent batteries and to recover valuable materials.

Current commercial LIB recycling techniques, including hydro-metallurgical and pyrometallurgical processes, focus on reclaiming the metal elements (Li, Co, Ni, and Mn) contained in their cathodes.[4] However, the anode material (mainly graphite), which accounts for up to 20% of the total weight of a typical LIB cell,[5] is either burned or landfilled.[6] This non-ideal practice not only releases large amounts of greenhouse gasses, but also inefficiently processes a material that otherwise still holds the ability to provide electrochemical energy, which is much more efficient than combustion. Industry does not currently practice graphite cycling partially due to its relatively low cost ($6 \sim 10$ \$ kg^{-1}) compared to transition metal oxide cathode(e.g., ~20 \$ kg^{-1} for $LiNi_{0.5}Co_{0.2}Mn_{0.3}O_2$).[7] A sustainable process for anode recycling that maximizes the overall value with minimal operating cost is highly desired.

Generally, the capacity degradation of LIBs is mainly attributed to the loss of Li inventory with some structure changes, which are resulted from the formation of solid-electrolyte interphase (SEI) on the surface of graphite particle, chemical destruction of cathode materials and mechanical failure due to repeated volume changes in both electrodes.[8] Notably, in spite of capacity degradation from spent graphite anodes, their morphology and bulk structure are often maintained.[9–12] Some prior efforts have been made to rejuvenate spent graphite electrodes through the removal of SEI using strong caustic acids (e.g., HCl, H_2SO_4) followed by high-temperature annealing.[13–15] However, the use of strong acids poses a secondary pollution concern. In addition, even with using extremely high annealing temperature (e.g., >1500 °C), the capacity of recycled graphite remained inferior to the pristine ones,[15,16] making them inappropriate for making high quality new cells.

Herein, we report a direct regeneration approach by completely healing the surface and bulk defects of spent graphite particles. An in situ formed boron (B) based surface coating further improves the thermal and electrochemical stability of the regenerated graphite and restricts the surface area, leading to the high Li-storage capacity and excellent cycling stability. Combining advanced microscopic and spectroscopic techniques, we discovered that although thermal annealing after removing SEI may resume the majority of the capacity of spent graphite, the residual Li trapped in the bulk of graphite particles cannot be completely removed by such a conventional process. The remaining composition defects and the increased surface area of graphite particles are likely responsible for the performance gap between pristine graphite and the recycled ones using common approaches. We further showed that using a pretreatment with boric acid solution followed by a short annealing at moderate temperature, the residual Li trapped in the bulk of graphite particles can be completely removed. The use of non-volatile and non-toxic boric acid in the recycling process shows significant advantage over other caustic acids such as HCl and H_2SO_4. Compared with previous approaches, this new recycling process produces more active graphite particles with stabilized

*Electrochemical Society Student Member.
**Electrochemical Society Member.
***Electrochemical Society Fellow.
[z]E-mail: p1xu@eng.ucsd.edu; zhengchen@eng.ucsd.edu

surface, which are responsible for the high electrochemical performance and excellent cycling stability. This study provides greener and more efficient route for sustainable recycling of spent LIB anodes to reach the quality of pristine high-performance graphite.

Materials and Methods

Anode material harvesting.—Degraded graphite powder from cycled LIB anode was harvested from a spent pouch cell (General Motor's Chevrolet Volt EV cell, 20Ah). After manual disassembling, the anode strips were rinsed with dimethyl carbonate (DMC) before the graphite powder was scrapped from the copper current collector. The collected graphite powder (C-Graphite) was further washed with a small amount of N-methyl-2-pyrrolidone (NMP) under stirring and mild heating (80 °C) for 5 h to dissolve the polyvinylidene fluoride (PVDF) binder and separate carbon black conductive agent. After centrifuging at 3500 rpm for 5 min, the C-Graphite precipitation was then washed with distilled water. The black powder collected from a second centrifuging was dried under vacuum at 80 °C for 12 h. The obtained graphite was designated as washed graphite (W-Graphite).

Graphite regeneration.—The graphite regeneration was conducted by treating the W-Graphite in a boric acid solution followed by short thermal annealing. Briefly, the 1 g of W-Graphite was dispersed in a 2 ml of 5 wt.% boric acid solution, which was then dried under at 80 °C for 12 h. The dried graphite was then sintered in a nitrogen atmosphere for 1 h at 750 °C (B-750C-Graphite), 850 °C (B-850C-Graphite), 950 °C (B-950C-Graphite), and 1050 °C (B-1050C-Graphite), respectively. For comparison, W-Graphite was also sintered without any coating or doping, which was designated as sintered graphite (S-Graphite). These samples were sinteredat 750 °C (S-750C-Graphite), 850 °C (S-850C-Graphite), 950 °C (S-950C-Graphite), and 1050 °C (S-1050C-Graphite) for 1 h, respectively.

Materials characterization.—The morphology of the graphite particles was characterized using SEM imaging (FEI XL30). The crystal structure of the powders was examined by XRD on a Bruker D2 Phaser diffractometer (Cu Kα radiation, $\lambda = 1.5406$ Å). The XPS measurement was performed with Kratos AXIS Ultra DLD with Al Kα radiation to detect the elemental valence states. Specific surface areas of the samples were measured using the BET method with an Autosorb IQ, Quantachrome ASIQM. STEM-EDS mapping was performed on primary particles using a JEOL JEM-2800 at annular dark field (ADF) mode. All ADF images were acquired at 200 kV with a beam size of ≈5 Å. STEM-EELS was performed on JEOL JEM-ARM300CF at 300 kV, equipped with double correctors. To minimize possible electron beam irradiation effects, EELS spectra were acquired from areas without pre-beam irradiation.

Electrochemical characterization.—Graphite electrodes were prepared by mixing different graphite samples, PVDF, and Super P with a weight ratio of 8:1:1 in NMP solvent under stirring for 90 min to obtain a homogenous slurry, which was then cast onto a 12 μm thick copper foil followed by vacuum drying at 120 °C for 6 h. The electrodes were cut into 12 mm diameter discs, calendered, then assembled into half cells with lithium metal as counter electrode and LP40 electrolyte (1 M $LiPF_6$ in EC/DEC). Typical mass loading of graphite electrodes was controlled at ~5 mg cm^{-2}. The half-cell cycling was carried out by constant current charging and discharging at different rates from 0.01 to 1.5 V with a LANDT multi-channel battery cycler. Electrochemical impedance spectroscopy (EIS) tests were performed in the frequency range of 10^6 Hz to 10^{-3} Hz with a signal amplitude of 10 mV by using a Metrohm Autolab potentiostat.

Results and Discussion

To demonstrate our recycling approach, spent pouch cells (20Ah per cell) from a General Motor's Chevrolet Volt EV were disassembled in an argon-filled glovebox. Degraded graphite powders were harvested from the anodes following the procedure described in the experimental section. The collected spent graphite powders (denoted as "C-Graphite") were subject to different regeneration processes, including washed with N-Methyl-2-pyrrolidone (NMP) and water (denoted as "W-Graphite"), sintering after prior washing (denoted as "S-Graphite"), and washed with boric acid solution followed by short sintering (denoted as "B-Graphite").

First, scanning electron microscopy (SEM) imaging was applied to characterize the morphology of C-, W-, S- and B-Graphite. Figures 1a–1d show the SEM images of the four samples with different magnifications. Generally, all the samples exhibited irregular cobblestone-like shapes, typical synthetic graphite, with sizes ranging from 10 to 30 um, which indicates that the spent graphite did not undergo considerable morphological changes after cell cycling and any regenerative processing. As displayed in Fig. 1c, some bright spots could be observed on the surface of S-graphite, which might be associated to the decomposition products of the residual SEI. However, the B-Graphite shows a clean surface, which implies that the SEI was completely removed by the boric acid and following short annealing.

The crystal structure of cycled and regenerated graphite materials was further examined by X-ray diffraction (XRD) (Fig. 1e). It should be noted that the C-Graphite still displayed typical diffraction peaks of highly ordered graphite with the hexagonal crystal structure (JCPDS#75–2078), which suggests the promise of a direct regeneration approach for the spent graphite. Besides, no characteristic peaks from potential impurities (e.g., binder, conductive agent, copper from current collector, or SEI components) were observed. The crystallinity of graphite after sintering (S-Graphite and B-Graphite) was notably enhanced, which is reflected from the reduced peak broadening (full width half maximum, FWHM) in Table I. From the enlarged view of the (002) peak, a left shift for C-, W- and S-Graphite was observed. After treatment by boric acid solution followed by short annealing, the peak shifted back to the location similar to the pristine sample. According to the Bragg equation ($2d\,sin\theta = n\lambda$),[17,18] the interlayer distances for (002) plane (d_{002}) can be determined (Table I). It was found that the d_{002} of C-Graphite (3.359 Å) is slightly larger than the standard value (3.350 Å) of typical graphite,[19] which may be resulted from the residual Li between the graphite layers after long-term cycling. The spacing of W-Graphite maintained 3.360 Å, which indicates that the residual Li cannot be fully removed by the simple washing step. After sintering, the d_{002} increased to 3.366 Å, implying the expansion of graphite interlayers in the heating process. This might be due to the conversion of the bulk Li to $LiOH/Li_2CO_3$ after washing step,[20] which decomposed and released H_2O/CO_2 during sintering, enlarging the interlayer spacing. By comparison, it was found that the d_{002} of B-Graphite returned to 3.349 Å, which suggests that residual bulk Li has been largely extracted during the process.

X-ray photoelectron spectroscopy (XPS) measurement was further performed to analyze the surface composition of the graphite materials. Figure S1 (available online at stacks.iop.org/JES/167/160511/mmedia) depicts the survey spectra with the corresponding composition listed in Table SI. Specifically, 3.7 at.% of F and 4.2 at.% of Li were detected in the C-Graphite, which may be from binder (PVDF) and lithium salt (e.g., LiF) in SEI. The observation of 0.7 at.% of La in the graphite anode is probably from the cathode side (a mixture of $LiMn_2O_4$ and $LiNi_{1-x-y}Mn_xCo_yO_2$), which is a common dopant element for improving stability of cathode materials.[21–23]

Table I. Physical parameters of (002) peaks of C-, W-, S- and B-Graphite.

Sample	Interlayer Distance (Å)	FWHM (cm^{-1})
C-Graphite	3.359	0.277
W-Graphite	3.360	0.322
S-Graphite	3.366	0.238
B-Graphite	3.349	0.240

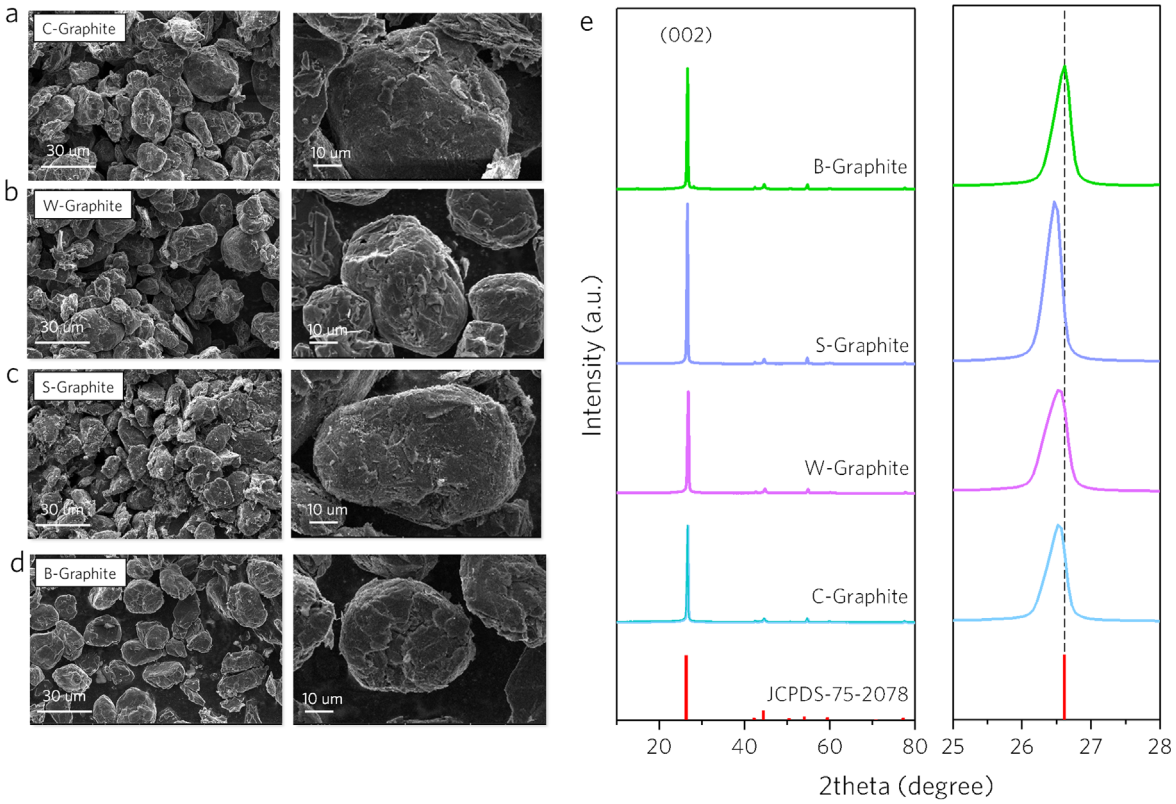

Figure 1. SEM images (a) -(d) at different magnifications and XRD patterns (e) of C-, W-, S- and B-Graphite.

After washing with NMP and distilled water, all the F, Li and Co signals were almost undetectable, indicating that the surface impurities associated with SEI products were removed. After annealing, no apparent change in composition was observed for S-Graphite. Notably, for the sample pretreated with boric acid followed by short annealing, 4.5 at.% of B coupled with 4.5 at.% of Li were detected on the surface of graphite particles, suggesting that the graphite surface was modified during the processing. The formation of B can be due to the existence of Li (in the form of LiOH, Li_2CO_3 etc.) with H_3BO_3, which will react in the following pathways.[24–26]

$$3LiOH + H_3BO_3 \rightarrow Li_3BO_3 + 3H_2O \quad [1]$$

$$Li_2CO_3 + 6H_3BO_3 \rightarrow 2LiB_3O_5 + CO_2 + 9H_2O \quad [2]$$

Although determining the exact composition can be difficult, local distribution of Li and B can be clearly identified (to be discussed later).

High-resolution XPS spectra of the C1s, O1s, and B1s of C-, W-, S-, and B-Graphite are shown in Fig. 2. The C1s spectra of all the samples were fit into three peaks located at 284.8, 285.9, and 289.9 eV, which are assigned to C–C/C=C, C–O, and C=O interactions, respectively (Fig. 2a).[27] The O1s spectra (Fig. 2b) of the C-, W-, and B-Graphite show similar fitting peaks at 531.98 and 533.62 eV, corresponding to C=O and C–O, respectively. However, a small peak associated with Li_2O (529.34 eV) was detected for S-Graphite, which is probably attributed to the decomposition of the remaining SEI.[28] This is consistent with the observed surface species in the SEM images (Fig. 1c) shown previously. Overall, the surface O content reduced from 7.5 at% (C-Graphite) to 2.4 at% for B-Graphite, while W- and S-Graphite still showed 8.6 at% and 6.1 at% of O, respectively. Finally, the fine spectra of B1s were compared in Fig. 2c, where the B-Graphite showed a peak located at 190.4 eV, which can be ascribed to B–C bond,[29] further confirming that boron atoms are incorporated to the graphite during the regeneration processing. The B–C bond formation might originate from the carbon thermal reduction reaction of lithium boron oxides ($Li_xB_yO_z$).[30,31]

The surface distribution of B and Li elements were further probed by scanning transmission electron microscopy (STEM) combined with energy dispersive X-ray spectroscopy (EDS). The high-angle annular dark-field STEM (HAADF-STEM) images and corresponding electron energy loss spectroscopy (EELS) elemental mapping of all the graphite samples were shown in Figs. 3a–3d. Besides C and Li element were observed in the C-graphite (Fig. 3a), the EDS elemental mapping also detected O, F, P, and S elements (Fig. S2). The presence of F and P are likely associated with residual SEI, and the presence of S may originate from electrolyte additives present in the original cell. It should be further noted that the residual Li in the C-Graphite was quite significant, approaching an atomic fraction of 20% of the entire sample. Interestingly, from the uniform distribution of Li, it can be found that Li was not only present on the surface (surface-Li) but also within the bulk of the graphite particles (bulk-Li). The surface-Li is commonly considered as a part of the residual SEI, which typically consists of an inner layer of inorganic Li compounds and an outer layer of organic Li compounds.[32] The observation of a large amount of residual Li in the bulk of C-graphite is probably because some Li^+ ions cannot be extracted out from the graphite interlayers due to kinetics restriction as well as dead Li^+ irreversibly trapped in the structure defects such as turbostratic disorder, grain boundaries, unorganized carbons.[33,34] It follows that when regenerating spent graphite materials, the bulk-Li must be removed completely to fully recover the electrochemical performance of the material. As shown in the Li elemental mapping in Figs. 3b and 3c, even after washing and sintering, only ~10% surface-Li was removed (Fig. 3e) during processing (W- and S-Graphite). By contrast, when the C-Graphite was treated with boric acid followed by a short sintering step, the bulk-Li was completely removed and only ~4.5% of Li remained on the surface, as shown in Fig. 3d.

The chemical bonding information was further determined by EELS. Figures 4a–4c depict the EELS spectra of the characteristic K-shell ionization edges of Li, C and B, respectively, where the four samples showed similar Li EELS spectra with a broad peak,

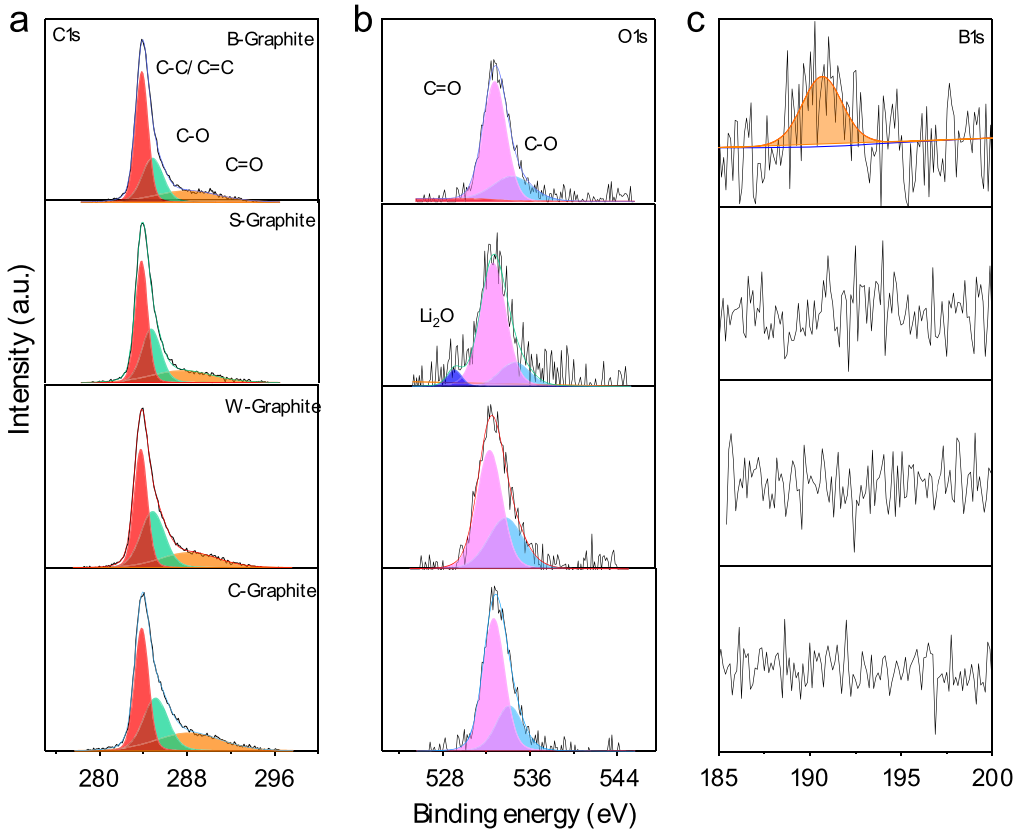

Figure 2. High resolution XPS spectra of C1s (a), O1s (b) and B1s (c) of C-, W-, S- and B-Graphite.

however, the peaks from Li compounds (Li_2O, Li_2CO_3, LiF, LiC_x, etc.) typically overlap, and are difficult to distinguish.[35] Overall, the C K-edge spectra of the four samples are analogical, which showed a first peak corresponding to the 1s-π* antibonding orbital, followed by a wider band attributed to the 1s-σ* antibonding orbital, indicating a well-graphitized sp^2-hybridization structure.[36] Notably, the peak intensity based on the Li K-edge for each sample was normalized. Consequently, the peak intensity evolution of C K-edge in different samples can represent the C/Li atomic ratio. The much higher C K-edge intensity for the borate treated sample qualitatively indicates the effective bulk Li removal compared with the cycled sample.

In addition, the EELS spectrum of the B K-edge was also collected and shown in Fig. 4c, where two intense peaks were observed. The first peak at 190.4 eV is ascribed to the 1s-π* resonance, and the second peak at 199.5 eV is due to the 1s-σ* interactions, which demonstrates the presence of the sp^2 and sp^3 hybridization of boron in the hexagonal boron/carbon conformation.[37,38] Hence, it was concluded that the B element on the surface of B-Graphite was bonded with carbon atoms, forming a BC_x compound, which is consistent with the XPS result in Fig. 2c. The B-doping on the graphite edge provides one less electron compared with pure graphite material. The Li can be considered as an electron donor to fill the unoccupied states,[34,39] which accordingly can lead to extra lithium absorbed on the edge of graphite particles (Fig. 3d).

The surface area, a critical parameter affecting the stability of LIB anode, of all S-Graphite and B-Graphite samples obtained at different annealing temperatures was probed by N_2 adsorption/desorption experiment (Figs. S3–S4). The Brunauer–Emmett–Teller (BET) surface area (S_{BET}) of S-Graphite increased from 3.62 to 7.84 $m^2\ g^{-1}$ as the annealing temperature increased from 750 to 1050 °C. In contrast, the S_{BET} of B-Graphite reduced from 3.65 to 3.06 $m^2\ g^{-1}$ for the same change of annealing temperature. These results agree with the prior XRD data (Table I, Fig. 1) that the interlayer spacing of S-Graphite expanded compared with typical graphite while the spacing remained the same for B-Graphite. They are also consistent with the XPS results that the surface O content of S-Graphite is significantly higher than that of B-Graphite. Therefore, the surface modification of graphite with boron can significantly restrict the increase of surface area with the elevation of sintering temperature compared with S-Graphite (Fig. S5).

The thermal stability of graphite materials was further explored by thermogravimetric analysis (TGA), which was carried out by heating from room temperature to 900 °C with a heating rate of 10 °C min^{-1} under an oxygen atmosphere. Meanwhile, the differential scanning calorimetry (DSC) was collected as well, which is favorable to further determine the composition of graphite materials. The TGA and DSC curves were plotted in Fig. 4d. The C-Graphite exhibited a weight loss of ~2 wt.% between 100 °C and 350 °C, coupling with a broad DSC thermogram peak in this temperature window, which can be ascribed to the evaporation of physically adsorbed water.[40] The weight loss of 4 wt.% between 350 °C to 550 °C, accompanying with a DSC thermogram peak located at ~475 °C, can be assigned to pyrolysis of PVDF binder.[41,42] A clear DSC thermogram peak at ~570 °C associated with LiOH can be observed.[43] However, the related weight loss cannot be quantified accurately because it was merged with the dramatic weight decrease caused by the combustion of carbon. After washing, the DSC thermogram peak related to PVDF disappeared, suggesting the binder was removed from the graphite sample, which is consistent with the XPS result. The thermogram transition at ~570 °C indicated that the lithium in W-Graphite was present as LiOH. For the S-Graphite, only a sharp endothermic peak at ~760 °C associated with the combustion of graphite appeared. It should be noted that there was a remaining 8 wt.% of substance after graphite was burned out of. It is considered to be Li_2O converted from LiOH, which can be thermally stable over the measured temperature range.[43] Interestingly, the B-Graphite was found to be stable up to 700 °C, which is likely due to the stabilizing effect of boron on the surface of graphite.[44,45] In this sample, atmospheric

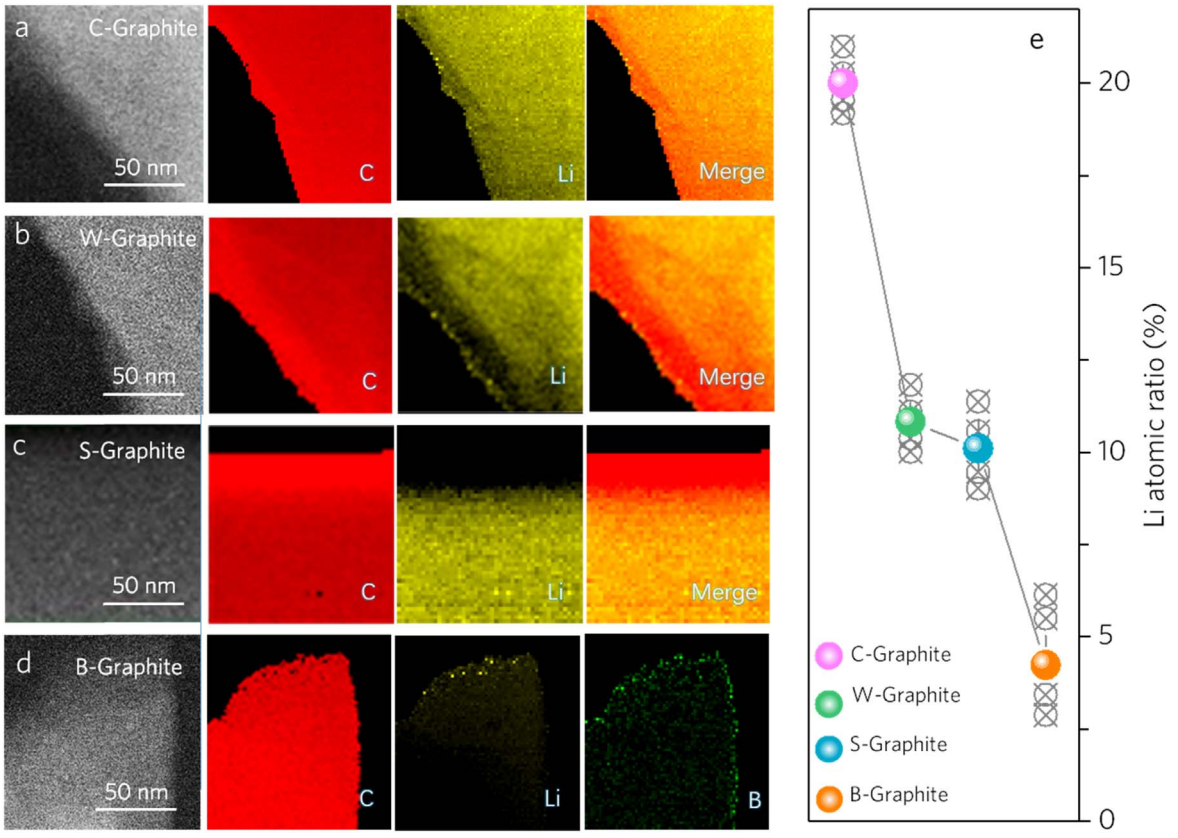

Figure 3. HAADF-STEM images and EELS elemental mapping of C-, W-, S- and B-Graphite (a)–(d); Normalized Li concentration quantified from EELS mapping result of different graphite samples (e).

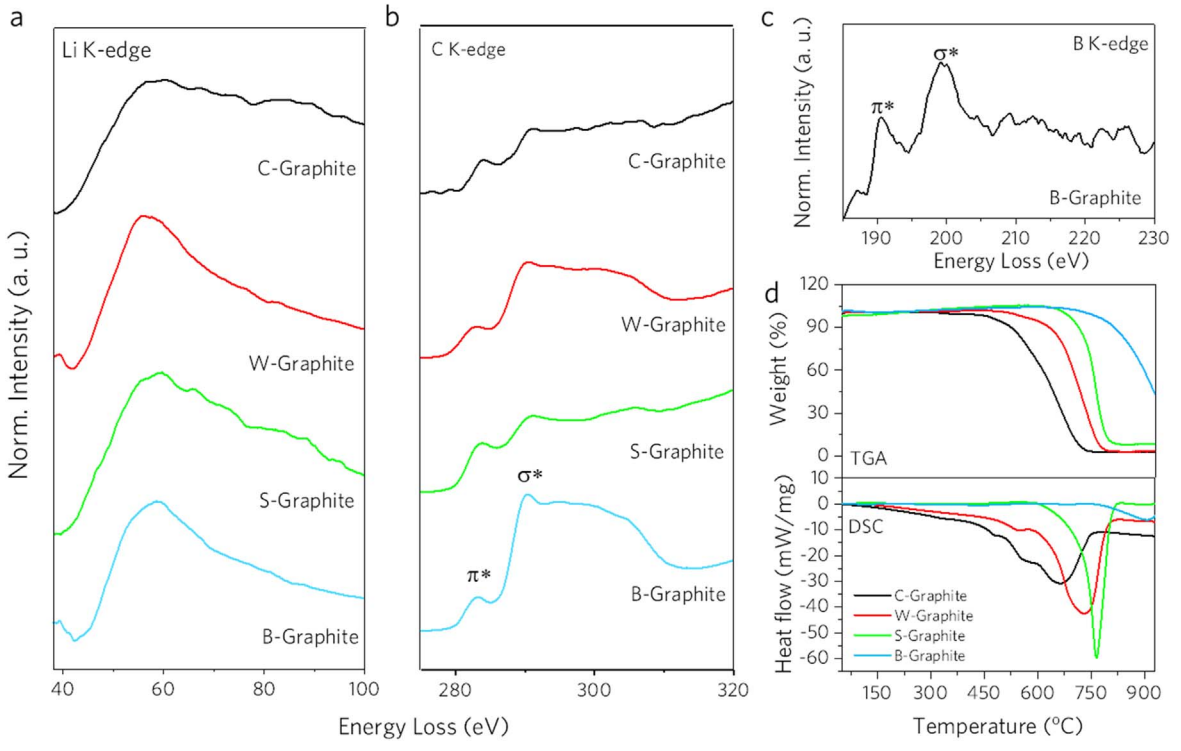

Figure 4. STEM-EELS of Li K-edge (a), C K-edge (b) of C-, W-, S- and B-Graphite and B K-edge of B-Graphite (c); TGA/DSC curves of C-, W-, S- and B-Graphite (d).

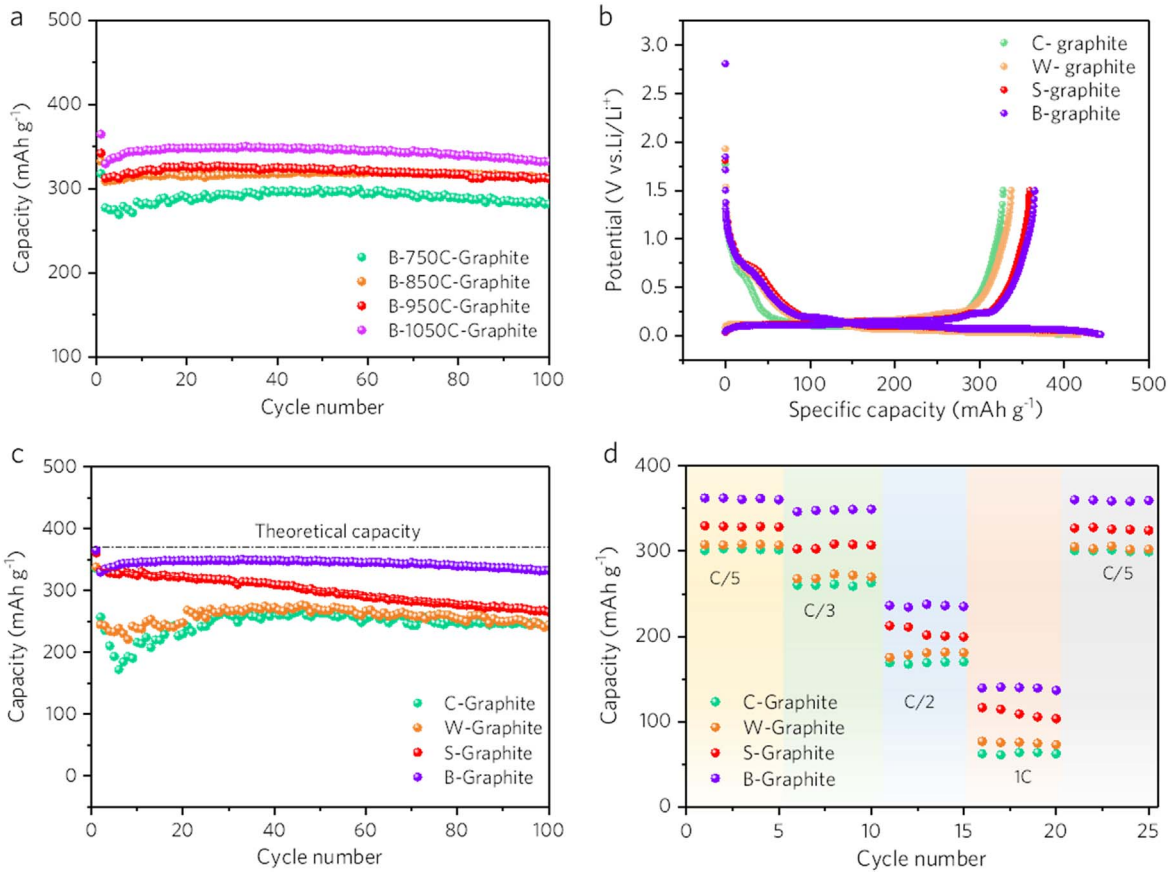

Figure 5. Cycling stability of B-graphite sintered at different temperatures (a); voltage profiles (b), cycling stability (c) and rate capability (d) of C-, W-, S- and B-Graphite obtained a 1050 °C sintering.

oxygen would preferentially react with boron due to its lower electronegativity when compared to carbon, forming boron oxide. The boron oxide could serve as a physical diffusion barrier, reducing the oxidation rate of graphite.[46] Therefore, the B-Graphite was not completely burned out even it was heated to 900 °C and the corresponding thermogram peak did not show up completely.

The electrochemical performance of cycled and regenerated graphite was studied with half-cells under the galvanostatic cycling. The cycling stability of the B-graphite sintered at different temperatures was tested with a C/10 activation cycle and 100 subsequent cycles at C/3 (Fig. 5a). The capacity of all samples showed an increasing trend during the initial cycles due to activation process and then tended to stabilize. The B-Graphite sintered at 1050 °C exhibited an increased average capacity of 332 mAh g^{-1} (at C/3) compared with the samples sintered at lower temperatures (279 mAh g^{-1} for B-750C-Graphite, 310 mAh g^{-1} for B-850C-Graphite and 312 mAh g^{-1} for B-950C-Graphite), which might be attributed to the increased ordering of graphite layers and decreased structural defects.

The charge and discharge curves of C-, W-, S-, and B-Graphite were compared in Fig. 5b. All the samples showed a small plateau between 0.8 V–0.6 V in the discharge process, which is associated with the formation of SEI, and a long plateau between 0.2 V to 0.02 V, which can be assigned to intercalation of Li^+ in graphite interlayers. It should be noted that the first plateau of the S-Graphite was the longest among all the samples, accounting for 5% of the total discharge capacity, which leads to a lower Columbic efficiency (80%) than the other three samples (83% for C-Graphite, 81% for W-Graphite, 82% for B-Graphite). This is consistent with the highest S_{BET} of S-Graphite among all the graphite samples. Despite this efficiency, the C-Graphite exhibited a reduced ability to host fresh Li^+ due to the residual dead Li in the bulk graphite, which occupied the active sites b As displayed in Fig. 1c etween the graphite interlayers, leading to a reduced discharge capacity of only 295 mAh g^{-1}.

The cycling stability and rate capability of the C-, W-, S- and B-Graphite were further compared (Figs. 5c and 5d). The S-Graphite was found to deliver a capacity of 331 mAh g^{-1} at a C/3 rate, however, only 265 mAh g^{-1} was retained after 100 cycles. A possible cause is the increased specific surface area after sintering at 1050 °C (Fig. S4), leading to more parasitic reactions and gradual capacity degradation.[47] It was interesting to find that the surface doping of boron not only improved the initial capacity to 330 mAh g^{-1} but also retained the capacity to be 333 mAh g^{-1} after 100 cycles. This is probably because after subtraction of the bulk-Li during the regeneration process, the occupied active sites between the graphite interlayers and grain boundaries were released, suggested by the resumed interlayer spacing (Table I). Since the removal of bulk residual Li reopens the channels for Li transport, the rate capability was enhanced as well (Fig. 5b). The average capacity delivered by the B-Graphite was 362, 348, 234 and 140 mAh g^{-1} at rates of 0.2 C, 0.3 C, 0.5 C and 1 C, respectively. Furthermore, when the rate was returned to 0.2 C, a capacity of 358 mAh g^{-1} was retained. By comparison, when the rate was increased to 1 C, only 108, 74 and 64 mAh g^{-1} was exhibited by the S-Graphite, W-Graphite and C-Graphite, respectively.

EIS was then implemented to investigate the electrochemical kinetics of cycled and regenerated graphite martials. The Nyquist plots were plotted in Fig. S6, which were fitted with the equivalent circuit (inset of Fig. S6) to get quantitative values of resistances. R_s, R_{SEI}, and R_{ct} refer to the internal resistance of electrode and electrolyte, SEI film resistance, and charge transfer resistance, respectively. CPE (constant phase element) is used to supplement non-ideal capacitor behavior. *W* is the Warburg impedance, which is

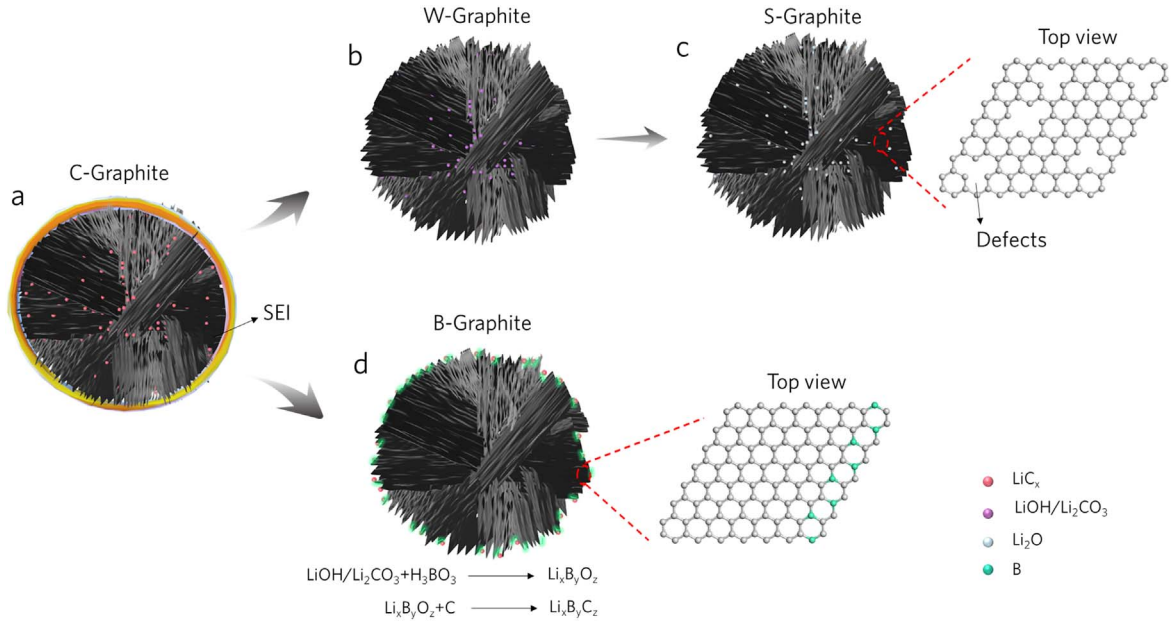

Figure 6. Scheme of C-Graphite(a) after different treatment: washing (b), sintering after washing(c) and boric treatment followed by sintering (d).

also known as the diffusion resistance. The C-Graphite displayed the largest R_{ct} (16.3 Ω), which is likely attributed to the remaining impurity species in the cycled graphite material. After washing, the R_{ct} of W-Graphite was reduced to 14.6 Ω, which is owing to the removal of PVDF binder from the graphite particle. After sintering at 1050 °C, although the R_{ct} was further reduced to 13.6 Ω, it was still much higher than that of B-Graphite (8.6 Ω). This might be due to the dead Li residual inside the graphite particle, which would lead to high electrochemical polarization, resulting in capacity loss especially at high charging/discharging rate. The above results are consistent with the established understanding of graphite anode that the interface of graphite and electrolyte is the first barrier that the Li ions need to diffuse through, and the edge features and disordered carbon structure significantly affect the Li^+ intercalation behavior. The B-doping surface modifies the local electronic structure and tailor interface properties, which correspondingly enhances the rate and durability.[39]

The above-discussed mechanisms of the various regeneration processes are summarized and illustrated in Fig. 6. It is discovered that the reversible Li^+ loss accounting for the battery capacity decay is attributed to not only the formation of SEI and but also the Li^+ trapped in the graphite bulk (turbostratic structures, edge sites, grain boundaries, etc.), as shown in Fig. 6a. After washing with NMP and distilled water, the surface SEI can be largely removed. However, a significant portion of the bulk Li likely remains, occupying or blocking the active sites of graphite interlayers and disordered carbon structures, which sacrifice the usable capacity (Fig. 6b). After further sintering at high temperature, the specific surface area was increased, which might be caused by induced defects by the removing residual bulk-Li (Fig. 6c). In contrast, the boric acid treatment followed by sintering not only completely extracts dead Li in the bulk structure of graphite particles, but also modifies the graphite surface with boron doping, which largely improves the thermal stability and minimize the surface area, leading to high electrochemical activity and cycling stability.

Conclusions

In summary, we demonstrated efficient upcycling of spent graphite anodes by leveraging fundamental understanding of the evolution of structural and compositional defects in different regeneration processes. By combining various advanced characterization methods, we clearly identified that the residual Li in the bulk of degraded graphite particles is mainly responsible for the capacity deficiency of regenerated spent graphite by simple washing and sintering process. Applying boric acid solution treatment followed by short annealing we demonstrated complete regeneration of fine structures of spent graphite as well as introducing functional B-doping, which provides both high electrochemical activity and excellent cycling stability. Considering the low cost, non-volatile and non-caustic nature of boric acid as well as the simple process, our approach may represent a more promising direction for green and sustainable recycling of spent LIB anodes.

Acknowledgments

This work was supported by US National Science Foundation via Award CBET-1805570 and US Department of Energy via ReCell Center, Vehicle Technologies Office, specifically from Samuel Gillard, Peter Faguy, and David Howell. . We acknowledge the UC Irvine Materials Research Institute for the use of the (S)TEM facilities, funded in part by the NSF Major Research Instrumentation Program under grant CHE-1338173. Part of the work used the UCSD-MTI Battery Fabrication Facility and the UCSD-Arbin Battery Testing Facility.

Authors Contribution

Z. C. designed the experiment and directed the project. B. M. and I. R. carried out the synthesis and electrochemical evaluations. D. X. performed the BET test. Y. Z. and J. G. conducted the TGA measurement. P. X. performed part of the electrochemical test and analyzed the data. M. C. and Y. M. assisted the experiment design. H. G. and D. Z. conducted DSC measurement. M. Z. collected and analyzed the (S)TEM and EELS data. P. X. and Z. C. wrote the manuscript. J. H. revised the manuscript. All authors discussed the results and commented on the manuscript.

ORCID

Ying Shirley Meng https://orcid.org/0000-0001-8936-8845
Zheng Chen https://orcid.org/0000-0002-9186-4298

References

1. P. Meister, H. Jia, J. Li, R. Kloepsch, M. Winter, and T. Placke, *Chem. Mater.*, **28**, 7203 (2016).
2. T. Yamanaka, T. Abe, K. Nishio, and Z. Ogumi, *Journal of Materials Chemistry A*, **6**, 11005 (2018).

3. M. Chen, X. Ma, B. Chen, R. Arsenault, P. Karlson, N. Simon, and Y. Wang, *Joule*, **3**, 2622 (2019).
4. R. E. Ciez and J. F. Whitacre, *Nature Sustainability*, **2**, 148 (2019).
5. L. Du, W. Du, H. Ren, N. Wang, Z. Yao, X. Shi, B. Zhang, J. Zai, and X. Qian, *Journal of Materials Chemistry A*, **5**, 22527 (2017).
6. B. Moradi and G. G. Botte, *J. Appl. Electrochem.*, **46**, 123 (2016).
7. B. Huab and G. Tao, *Journal of Materials Chemistry A*, **3**, 20399 (2015).
8. N. Paul, J. Wandt, S. Seidlmayer, S. Schebesta, M. J. Mühlbauer, O. Dolotko, H. A. Gasteiger, and R. Gilles, *J. Power Sources*, **345**, 85 (2017).
9. C. R. Birkl, M. R. Roberts, E. McTurk, P. G. Bruce, and D. A. Howey, *J. Power Sources*, **341**, 373 (2017).
10. H. Wang, Y. Huang, C. Huang, X. Wang, K. Wang, H. Chen, S. Liu, Y. Wu, K. Xu, and W. Li, *Electrochim. Acta*, **313**, 423 (2019).
11. J. Zhang, X. Li, D. Song, Y. Miao, J. Song, and L. Zhang, *J. Power Sources*, **390**, 38 (2018).
12. M. B. Pinson and M. Z. Bazant, *J. Electrochem. Soc.*, **160**, A243 (2012).
13. L. Barbosa, F. Luna-Lama, Y. Gonzalez Pena, and A. Caballero, *ChemSusChem*, **13**, 838 (2020).
14. Y. Yang, S. Song, S. Lei, W. Sun, H. Hou, F. Jiang, X. Ji, W. Zhao, and Y. Hu, *Waste Manag*, **85**, 529 (2019).
15. X. Ma, M. Chen, B. Chen, Z. Meng, and Y. Wang, *ACS Sustainable Chemistry & Engineering*, **7**, 19732 (2019).
16. Y. Gao, C. Wang, J. Zhang, Q. Jing, B. Ma, Y. Chen, and W. Zhang, *ACS Sustainable Chemistry & Engineering*, **8**, 9447 (2020).
17. C. Ye, W. Tu, L. Yin, Q. Zheng, C. Wang, Y. Zhong, Y. Zhang, Q. Huang, K. Xu, and W. Li, *Journal of Materials Chemistry A*, **6**, 17642 (2018).
18. M. Lu, W. Han, H. Li, W. Shi, J. Wang, B. Zhang, Y. Zhou, H. Li, W. Zhang, and W. Zheng, *Energy Storage Mater.*, **16**, 163 (2019).
19. B. M. Way, J. R. Dahn, T. Tiedje, K. Myrtle, and M. Kasrai, *Physical Review B*, **46**, 1697 (1992).
20. R. L. Sacci, L. W. Gill, E. W. Hagaman, and N. J. Dudney, *J. Power Sources*, **287**, 253 (2015).
21. R. Yu, G. Wang, M. Liu, X. Zhang, X. Wang, H. Shu, X. Yang, and W. Huang, *J. Power Sources*, **335**, 65 (2016).
22. Q. Liu et al., *Nat. Energy*, **3**, 936 (2018).
23. D. Arumugam, G. P. Kalaignan, and P. Manisankar, *Solid State Ionics*, **179**, 580 (2008).
24. Z. Özdemir, G. Özbayoğlu, M. Kizilyalli, and A. Yilmaz, *Physicochemical Problems of Mineral Processing*, **38**, 321 (2004).
25. V. F. Stewner, *Acta Crystallogr.*, **B27**, 904 (1971).
26. Z. Shuqing, H. Chaoen, and Z. Hongwu, *J. Cryst. Growth*, **99**, 805 (1990).
27. M. Yi, Z. Shen, X. Zhang, and S. Ma, *J. Phys. D: Appl. Phys.*, **46**, 025301 (2012).
28. K. P. C. Yao, D. G. Kwabi, R. A. Quinlan, A. N. Mansour, A. Grimaud, Y.-L. Lee, Y.-C. Lu, and Y. Shao-Horn, *J. Electrochem. Soc.*, **160**, A824 (2013).
29. C. Xu, Y. Su, D. Liu, and X. He, *Phys. Chem. Chem. Phys.*, **17**, 25440 (2015).
30. C.-H. Jung, M.-J. Lee, and C.-J. Kim, *Mater. Lett.*, **58**, 609 (2004).
31. D.-Y. Yeom, W. Jeon, N. D. K. Tu, S. Y. Yeo, S.-S. Lee, B. J. Sung, H. Chang, J. A. Lim, and H. Kim, *Sci. Rep.*, **5**, 9817 (2015).
32. Y. Zhou et al., *Nat. Nanotechnol.* (2020).
33. K. Tatsumi, *J. Electrochem. Soc.*, **142**, 716 (1995).
34. J. R. Dahn, A. K. Sleigh, H. Shi, J. N. Reimers, Q. Zhong, and B. M. Way, *Electrochim. Acta*, **38**, 1179 (1993).
35. C. Funke and K. Chakrvadhanula Venkata Sai, "Characterisation of battery materials by electron and ion microscopy techniques: a review." *Physical Sciences Reviews*, **4**, 20170153 (2019).
36. L. Ci et al., *Nat. Mater.*, **9**, 430 (2010).
37. Y. Lin, Y. Zhu, B. Zhang, Y. A. Kim, M. Endo, and D. S. Su, *Journal of Materials Chemistry A*, **3**, 21805 (2015).
38. G. G. Fuentes, E. Borowiak-Palen, M. Knupfer, T. Pichler, J. Fink, L. Wirtz, and A. Rubio, *Physical Review B*, **69**, 245403 (2004).
39. C. Peng, M. P. Mercer, C.-K. Skylaris, and D. Kramer, *Journal of Materials Chemistry A*, **8**, 7947 (2020).
40. D. W. McOwen, D. M. Seo, O. Borodin, J. Vatamanu, P. D. Boyle, and W. A. Henderson, *Energy & Environmental Science*, **7**, 416 (2014).
41. Y. Cao, M. Liang, Z. Liu, Y. Wu, X. Xiong, C. Li, X. Wang, N. Jiang, J. Yu, and C.-T. Lin, *RSC Adv.*, **6**, 68357 (2016).
42. G. Zhang, Y. He, Y. Feng, H. Wang, and X. Zhu, *ACS Sustainable Chemistry & Engineering*, **6**, 10896 (2018).
43. H. Beyer, S. Meini, N. Tsiouvaras, M. Piana, and H. A. Gasteiger, *Phys. Chem. Chem. Phys.*, **15**, 11025 (2013).
44. J. Marx, H. Beisch, S. Garlof, and B. Fiedler, *Advanced Material Science*, **2**, 1–7 (2017).
45. Q. Wang, L.-Q. Chen, and J. F. Annett, *Physical Review B*, **54**, R2271 (1996).
46. X. Ma, Q. Wang, L. Q. Chen, W. Cermignani, H. H. Schobert, and C. G. Pantano, *Carbon*, **35**, 1517 (1997).
47. H. Wang, T. Ikeda, K. Fukuda, and M. Yoshio, *J. Power Sources*, **83**, 141 (1999).